Front. Mater. Sci. 2024, 18(4): 240702
https://doi.org/10.1007/s11706-024-0702-z

RESEARCH ARTICLE

Construction of single-atom copper-loaded iron-based MOF/carbon nitride nanosheet heterojunction for enhanced N_2 photofixation under visible light

Xinshan Rong (✉), Yuqing He, Ping Gao, Ting Sun, Xiangtong Zhou, and Zhiren Wu (✉)

School of Environment and Safety Engineering, Jiangsu University, Zhenjiang 212013, China

ABSTRACT: The utilization of photocatalytic nitrogen fixation, a process celebrated for its environmental friendliness and sustainability, has emerged as a promising avenue for ammonia synthesis. The rational design of photocatalysts containing single atoms and heterojunctions has been a long-standing challenge for achieving efficient nitrogen fixation. This study innovatively constructs composite catalysts integrating single-atom copper within metal–organic frameworks (Fe-MOF, NH_2-MIL-101) and carbon nitride nanosheet (CNNS). The nitrogen fixation efficiency of the Cu@MIL-CNNS heterojunction was 8 and 12 times those of the original MOF and CNNSs, respectively. Through detailed characterization, we unveil a unique charge transfer pathway facilitated by the synergy between single-atom copper and heterojunctions, highlighting the critical function of copper centers as potent active sites. Our findings underscore the transformative potential of single atomic sites in amplifying charge transfer efficiency, propelling advancements in the photocatalyst design.

KEYWORDS: single atom copper; photocatalytic nitrogen fixation; metal–organic framework; carbon nitride nanosheet

Contents

Received May 24, 2024; accepted September 28, 2024

E-mails: rxsmile@ujs.edu.cn (X.R.), zhirenwu@126.com (Z.W.)

1 Introduction

Ammonia (NH_3), as one of the indispensable chemicals, has been widely used in agriculture and industry [1]. In recent years, NH_3 has been used as an important source of fertilizers to secure food supplies and as a renewable transportation fuel, in addition to being an energy carrier and a sustainable fuel to achieve a global clean energy transition. However, the conventional Haber–Bosch process used for the industrial scale production of NH_3 has harsh reaction conditions that consume 1%–2% of the world’s energy supply annually and release about 1.5% of CO_2 into the environment [2]. Therefore, green and sustainable methods need to be developed to efficiently produce NH_3 under mild conditions. Over the past few decades, photocatalytic cured nitrogen has been one of the best choices due to its green, clean, and mild conditions, low-power consumption, and low-cost characteristics [3]. However, conventional photocatalysts, such as metal oxides and sulfides, exhibit poor ammonia synthesis activity due to their high carrier recombination efficiency [4–6]. Modification of these photocatalysts is often necessary to generate more photogenerated electrons and improve their efficiencies. A large amount of research has revealed that the efficiencies do not reach high levels yet due to the lack of sufficient active sites in binding and cleaving strong nonpolar N≡N triple bonds [7]. Meanwhile, single-atom catalysts have emerged as a promising solution with unique active centers and high atomic efficiencies that can enhance the catalytic performance of semiconductors [8]. The construction of heterojunctions is also an effective way to improve the carrier separation efficiencies of intrinsic semiconductors and generate more photogenerated electrons [9].

Metal monoatoms as active sites have attracted much attention for their maximum atom utilization efficiency, well-defined coordination environment, and excellent photocatalytic activity. It exhibits a low coordination state of metal atoms, usually with strong metal–carrier interactions, but the single atoms suffer from instability and susceptibility to agglomeration [10]. In contrast, metal–organic frameworks (MOFs) are special porous materials, composed of metal clusters and organic frameworks, with high porosity, large specific surface area, tunable functions, and potential catalytic capabilities [11]. MOFs have attracted extensive attention in various fields, including gas storage, separation, adsorption, sensing, catalysis, and photocatalysis [12–13]. In the field of photocatalysis, the high porosity and large surface area of MOFs provide ample sites for the adsorption of reactants, enhancing the light-harvesting efficiency and facilitating the catalytic conversion process [14]. The tunable nature of MOFs allows for the precise control of chemical and physical properties, enabling the optimization of light absorption and electron transfer dynamics [15]. Additionally, MOFs with their dispersed metal sites serve as effective platforms for anchoring single metal atoms, boosting the catalytic performance [16]. For example, Liu et al. successfully constructed a nickel monatomic immobilized zeolitic imidazolate framework-8 (ZIF-8), which had an ordered (macroscopic and microscopic) hierarchical pore structure and could photocatalytically reduce CO_2 to CO with effect, achieving high stability and activity with a CO yield of $4.2\ \mathrm{mmol \cdot g^{-1} \cdot h^{-1}}$ and an electron selectivity of 94% [17]. Wang et al. enhanced the photocatalytic performance in control of the level of defects in the bandgap for energy-level engineering and constructing unitary heterojunctions through MOF-based bionanocatalysts [18]. It was feasible to use MOFs with tunable structures and abundant chelating sites to anchor transition metals such as nickel and copper [19–20]. The encapsulation of atomically dispersed metal catalysts within the porous framework of MOFs offered a strategic approach to maximize accessible active centers, fostering robust interactions between metals and carrier materials [21]. Notably, the introduction of single-atom modifications could significantly alter the energy band structure of the catalyst, bestowing it with exceptional properties such as enhanced photo-absorption and expedited charge carrier separation [22]. These attributes collectively suggest that single-atom-loaded MOFs hold significant potential as co-catalysts for photocatalytic nitrogen fixation, an area of critical interest for the sustainable ammonia synthesis [23]. To load single atoms, the selection of MOFs with good energy band orientation is crucial. Various metal-centered MOFs have been studied in photocatalysts with a wide range of application pathways including Cu-, Zn-, Fe-, and Zr-MOFs [24–28]. Among them, iron-based MOFs offer better stability in organic solvents and water, as well as specific microstructures [29]. Currently, materials of Institut Lavoisier (MIL) and NH_2-MIL are two common types of Fe-based MOFs. The addition of $-NH_2$ groups to Fe-MOFs extends the p-conjugation and increases the visible-light absorption, which are key parameters for improving the conversion efficiency. Previous studies have shown that the combination of different semiconductors can effectively improve the photovoltaic performance and photocatalytic efficiency through providing fast transfer paths for charge carriers, facilitating close contact of interfaces between different materials [30].

Carbon nitride (CN) is a non-metallic polymer semiconductor that has been widely applied in the field of photocatalysis due to its suitable forbidden bandwidth and tunable band structure [31–32]. However, the low specific surface area (SSA) and rapid charge recombination (CR) rate limit its photocatalytic effect [33]. Designing MOF and CN heterojunction composites can increase the carrier mobility by increasing the light absorption range, tuning the SSA, and suppressing the electron–hole recombination rate. Heterojunctions consisting of MOF and CN have good results in enhancing the photocatalytic activity [34]. Cheng et al. prepared NH_2-MIL-125(Ti)-modified carbon nitride Cv-C_3N_4 with carbon vacancies, and the NO removal ratio of this compound reached 63%, which significantly improved the photocatalytic efficiency [35]. Lei et al. coupled and hybridized carbon nitride nanosheets (CNNSs) with MIL-88B(Fe), and the prepared nanocomposites formed heterojunctions that had relatively good performance in degrading methylene blue (MB) and reducing Cr(VI) under visible light [36]. Over the past few years, scientists have ventured into employing single atoms and fabricating heterojunctions to drive the photocatalytic synthesis of ammonia. However, devising efficacious and straightforward strategies to manipulate the energy band structure of these catalysts and optimize their heterojunction interfaces still remains an intricate puzzle, largely due to the multifaceted nature of the underlying reaction mechanisms. No method has yet been reported to analyze the charge transfer mechanism by coupling monoatomic loading and heterostructure construction, and to enhance photocatalytic nitrogen solidification performance through synergistic effects.

In this work, an impurity structure catalyst (Cu@MIL-CNNS) containing single-atom copper was used for effective photocatalytic nitrogen fixation. Anchored within an iron-based MOF, heterojunctions were formed in Cu@MIL-CNNS, which significantly facilitated the efficient separation and transfer of photo-induced charge carriers. A key advancement was observed in the capability of copper to modulate the MOF's band structure, thereby broadening its optical absorption spectrum. Moreover, copper was found to act as an active site, directly participating in catalytic reactions. Notably, superior photocatalytic efficiency and commendable recyclability have been demonstrated by Cu@MIL-CNNS among MOF-based photocatalysts, outperforming its constituent pure materials [37–38]. This work presents new opportunities for designing cost-effective and more active catalysts.

2 Experimental

2.1 Materials

All chemicals were from commercial sources and used without further purification. Anhydrous ethanol, urea, N,N-dimethylformamide (DMF), and 2-aminoterephthalic acid (NH_2-H_2BDC) were analytically pure and purchased from Sinopharm Chemical Reagent Co. Ltd. Ferric chloride hexahydrate ($FeCl_3{\cdot}6H_2O$) and copper chloride dihydrate ($CuCl_2{\cdot}2H_2O$) were purchased from Shanghai Aladdin Biochemical Technology Co. Ltd.

2.2 Catalyst fabrication

The synthesis process of Cu@MIL-CNNS heterojunctions is shown in Scheme 1. First, the porous iron-based metal–organic skeleton NH_2-MIL-101(Fe) (hereafter denoted as Fe-MOF) was prepared through the hydrothermal method reported in literature using $FeCl_3{\cdot}6H_2O$ and NH_2-H_2BDC as reaction materials [39]. Then $CuCl_2{\cdot}2H_2O$ was used as the copper source, and $CuCl_2{\cdot}2H_2O$ and Fe-MOF were stirred by the hydrothermal method to obtain sufficient interaction to introduce copper ions into the framework (Cu@MIL). On the other hand, ultrathin flocculated CNNSs were prepared through secondary calcination using urea as the raw material [40]. The prepared CNNSs and Cu@MIL were then added to a mixture of deionized water and ethanol in proportion to each other, and the visible light responsive Cu@MIL-CNNS composite catalyst was synthesized through simple stirring.

2.2.1 Synthesis of Fe-MOF

$FeCl_3{\cdot}6H_2O$ (2 mmol) and NH_2-H_2BDC (1 mmol) were dissolved in 30 mL dimethylformamide (DMF) solvent and stirred magnetically for 20 min. Then, they were

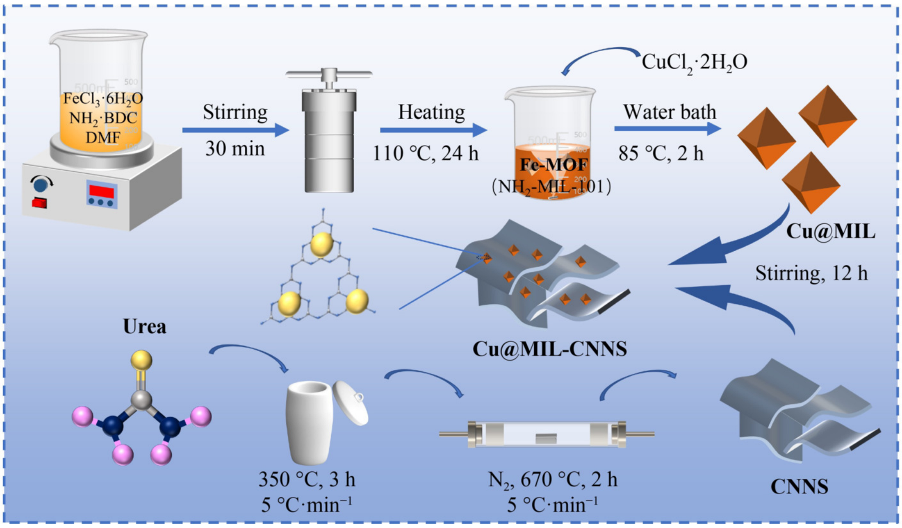

Scheme 1 Schematic diagram illustrating the synthesis of the Cu@MIL-CNNS heterojunction photocatalyst.

transferred to a Teflon-lined autoclave with a volume of 50 mL, and allowed to react for 24 h at 110°C. The resulting precipitate was centrifuged and washed three times with DMF and ethanol. Finally, the product was dried at 60 °C for 8 h.

2.2.2 Synthesis of CNNSs

Urea (20 g) was introduced into a covered quartz crucible, placed in a muffle furnace, and pyrolyzed at 350 °C for 3 h at a heating rate of 5 °C·min^{-1}. The product was ground into powders and placed in a covered quartz vessel and calcined in a tube furnace at 670 °C for 2 h under N_2 atmosphere at a heating rate of 5 °C·min^{-1}. The resulting precipitate was centrifuged, washed three times with DMF and ethanol, and dried at 60 °C for 8 h to obtain CNNSs.

2.2.3 Synthesis of Cu@MIL

Generally, 20 mg Fe-MOF, 0.2 mmol $CuCl_2·2H_2O$, and 50 mL DMF were mixed in a beaker, stirred continuously under the heating of a water bath at 85 °C for 2 h, cooled to room temperature, and then the solid was separated through centrifugation, washed thoroughly with DMF and anhydrous ethanol, and finally dried at 60 °C for 8 h to obtain Cu@MIL.

2.2.4 Synthesis of Cu@MIL-CNNS

30 mg of CNNSs were added into a solvent system containing a mixture of deionized water and ethanol with the volume ratio of 2:1 and then stirred at 25 °C for 0.5 h. The resulting solution was sonicated for 1 h, and then a certain amount of Cu@MIL was added and stirred at room temperature for 12 h. The loading mass ratios between CNNS and Cu@MIL were 10:1, 10:2, 10:3, and 10:4, which were hereafter denoted as Cu@MIL-CNNS-1, Cu@MIL-CNNS-2, Cu@MIL-CNNS-3, and Cu@MIL-CNNS-4, respectively.

2.3 Characterization

The structures, chemical compositions, and optical and electronic properties of the samples were studied. Details of the operational procedures were provided by ESM of Appendix.

2.4 N_2 photofixation measurement

In a CHX-3 photocatalytic reactor, N_2 photofixation measurements were conducted utilizing a 250 W xenon lamp. High-purity nitrogen gas (> 99.9%) was utilized as the nitrogen source, whereas deionized water acted as the proton donor. The reaction commenced by combining 50 mg of the sample with 100 mL of deionized water within the reactor. To maintain a constant temperature of 25 °C in the reaction system, a cooling jacket was employed, circulating water of the appropriate temperature. Under dark conditions, a continuous flow of N_2 gas was introduced into the reactor for a duration of 30 min. Following this, the reaction mixture was exposed to xenon lamps for a period of 2 h. Throughout the entirety of the experimental procedure, the solution was stirred using a magnetic stirrer to ensure the uniform dispersion of the catalyst. Post-exposure, the solution underwent filtration, and the concentration of ammonium ions (NH_4^+) was determined via the Nessler reagent method [41].

3 Results and discussion

3.1 Characterization

The analysis on crystal phases of the catalyst was performed through X-ray diffraction (XRD). The XRD results of the obtained MOF are consistent with those shown in Fig. 1. The theoretical calculation results in previous reports are consistent. There is strong evidence of the successful synthesis of Fe-MOF based on the results of the experiment [42]. However, the diffraction peak of copper was not detected, which may be due to the low loading of copper or the uniform and small particle size. Notably, the peak intensity of MOF was reduced due to the anchoring effect of copper, which could be attributed to doped Cu^{2+} ions, which destroyed the crystallinity of MOF and reduced the intensity of XRD peaks. In addition, the introduction of Cu^{2+} ions significantly shifted the main diffraction of MOF to the lower angular region by about 0.06° (inset in Fig. 1), and this shift to higher values has been reported in literature and is attributed to the contraction of the lattice when Fe^{3+} in Fe−O oxygen–oxygen clusters is replaced by the Cu^{2+} structure [20,43]. It indicates that some of Fe^{3+} ions are replaced by the introduced Cu^{2+} ions. For the Cu@MIL-CNNS-3 heterojunction, micropeaks of MOF and CNNSs can be observed, representing the construction of the heterojunction.

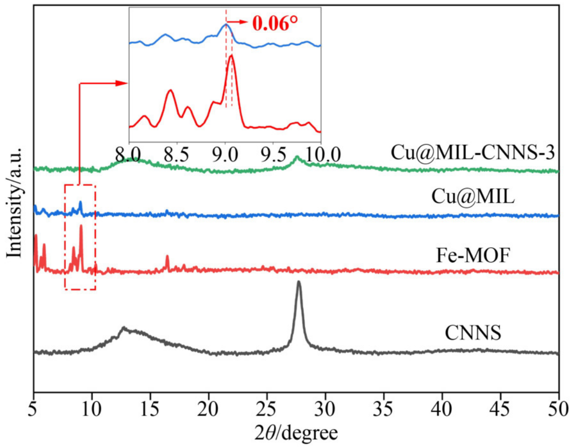

Fig. 1 XRD patterns of CNNS, Fe-MOF, Cu@MIL, and Cu@MIL-CNNS-3. Inset shows the offset of Cu@MIL with respect to the main diffraction of Fe-MOF.

Scanning electron microscopy (SEM) and transmitting electron microscopy (TEM) were performed for detailed analyses of structures and morphologies. Figure S1(a) (included by ESM of Appendix) shows that CNNSs are composed of ultrathin nanosheets displaying a highly fluffy and soft agglomerate morphology, which is further observed by the nearly transparent TEM image (Fig. 2(a)). Both Fe-MOF and Cu@MIL had a representative octahedral morphology similar to those in previous reports (Figs. S1(b) and S1(c) (included by ESM of Appendix) together with Figs. 2(b) and 2(c)), and no surface or interior particles were observed in Cu@MIL [44]. Moreover, the anchoring of copper did not cause any change in the morphology (Figs. 2(b) and 2(c)). For Cu@MIL-CNNS-3, CNNSs are tightly attached to the surface of Cu@MIL forming a tight interface (Figs. S1(d) and 2(d)), and a clear boundary between CNNSs and Cu@MIL can be observed from the images. This nanoscale heterojunction increases the SSA of the contact and contributes to the rapid involvement of carriers in the chemical reaction. The sample microscopic morphology was further investigated through high-angle annular dark-field scanning transmission electron microscopy (HAADF-STEM). Typical octahedral crystals of Fe-MOF wrapped with agglomerated lamellar CNNSs around them can be clearly seen in the dark-field STEM image (Fig. 2(e)). The effective complexation of Cu@MIL and CNNSs, as well as the uniform distribution of copper ions, is evidenced by elemental mapping images revealed in Fig. 2(f). To precisely determine the distribution of elements in the Cu@MIL-CNNS-3 sample, both energy dispersive X-ray spectroscopy (EDS) and inductively coupled plasma-atomic emission spectroscopy (ICP-AES) were employed. It was found that the copper content in the Cu@MIL-CNNS-3 sample measured via EDS was 1.68 wt.%, as shown in Fig. S2 (included by ESM of Appendix), while that via ICP-AES was 1.82 wt.%. Although there is a difference between such two values owing to different testing accuracies derived from various detecting instruments, the presence of copper ions can be confirmed.

X-ray photoelectron spectroscopy (XPS) was used to clarify compositions and chemical states of elements on surfaces of the prepared samples. As shown in Fig. 3(a),

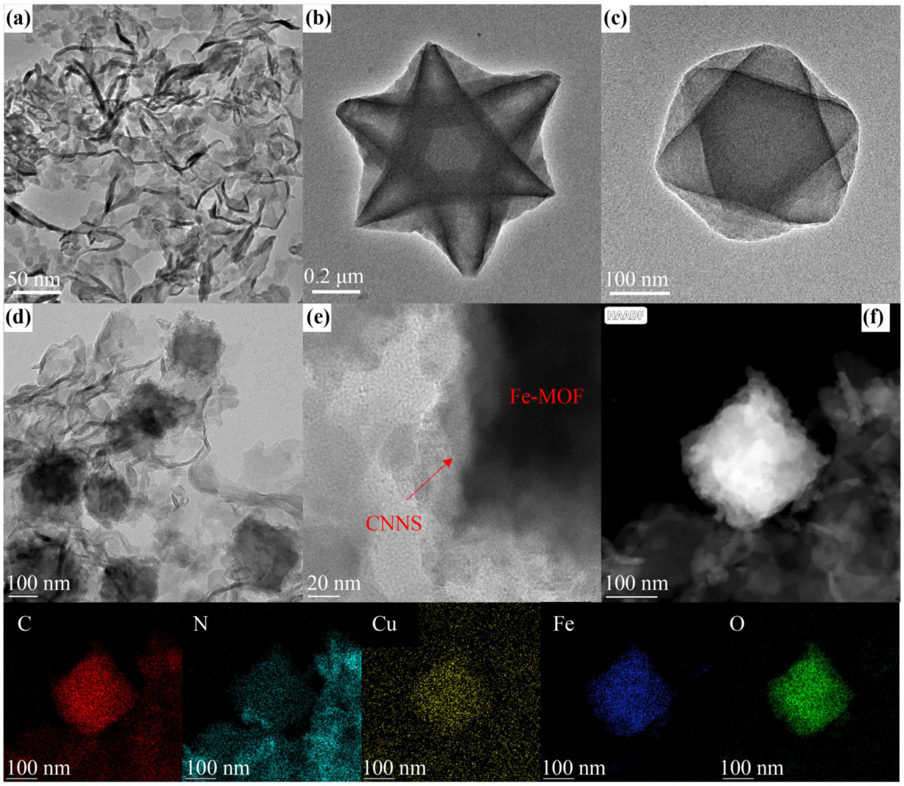

Fig. 2 (**a**)(**b**)(**c**)(**d**) TEM images of CNNSs (Panel (a)), Fe-MOF (Panel (b)), Cu@MIL (Panel (c)), and Cu@MIL-CNNS-3 (Panel (d)). (**e**) HAADF-STEM image of Cu@MIL-CNNS-3. (**f**) EDS elemental mapping images of Cu@MIL-CNNS-3.

C, N, O, and Fe were observed in the XPS spectrum of the Cu@MIL-CNNS-3 composite, while copper had no obvious peaks owing to its low content. According to Figs. S3(a) and S3(b) (included by ESM of Appendix), such characteristic peaks in Fig. 3(a) can be attributed to the presence of CNNS and Fe-MOF, providing strong evidence for the successful compounding between Fe-MOF and CN, consistent with SEM and XRD results. Furthermore, by employing *in-situ* XPS, the observed chemical shifts can be explained, shedding light on the charge transfer mechanism of Cu@MIL-CNNS-3 heterojunctions. Notably, in Fig. 3(b), peaks at 932.71 and 952.55 eV confirm the existence of Cu^+ ions as the predominant form of copper ions [45–46]. Figure 3(c) shows high-resolution Fe 2p XPS spectra of Fe-MOF, Cu@MIL, and Cu@MIL-CNNS-3 heterostructures. The presence of Fe^{3+} is demonstrated by peaks observed at 712.03 and 725.27 eV, corresponding to Fe $2p_{3/2}$ and Fe $2p_{1/2}$, respectively [47]. After doping with copper ions as well as composite CNNSs, slight negative shifts of Fe 2p peaks can be observed, mainly due to the increase in the electron density of Fe^{3+} possibly derived from the transfer of lone electron pairs of adjacent nitrogen atoms in CNNSs to Fe^{3+} sites in Cu@MIL as well as the presence of copper ions promoting the transfer of electrons on the surface and inside Fe-MOF [48]. Figure 3(d) provides high-resolution C 1s XPS spectra of Fe-MOF, Cu@MIL, and Cu@MIL-CNNS-3. The peaks at around 284.8 eV reveal the C−C bonding caused by foreign contaminations [49]. For Fe-MOF, peaks at 284.82 and 288.7 eV are attributed to the benzene ring of NH_2-BDC and the O−C=O group, respectively.

As revealed in O 1s XPS spectra delineated by Fig. 3(e), the elemental oxygen manifests three distinct configurations in Fe-MOF: as adsorbed oxygen, characterized with a binding energy of 530.57 eV; within water molecules encapsulated in NH_2-H_2BDC, evidenced at 531.96 eV; and as oxygen bound in the Fe−O bond, registered at 533.35 eV. As for N 1s, peaks at 398.26 and 399.62 eV are attributed to sp^2-bonded carbon and tertiary nitrogen (N−C_3) in the C−N≡C group of CNNSs, respectively, while peaks at 400.67 and 403.83 eV belong to the amino group (C−N−H) and the π excitation in CNNSs, respectively (Fig. 3(f)) [50]. When Cu@MIL and CNNSs are in contact, there is an interaction between them, promoting the transfer of electrons from CNNSs to

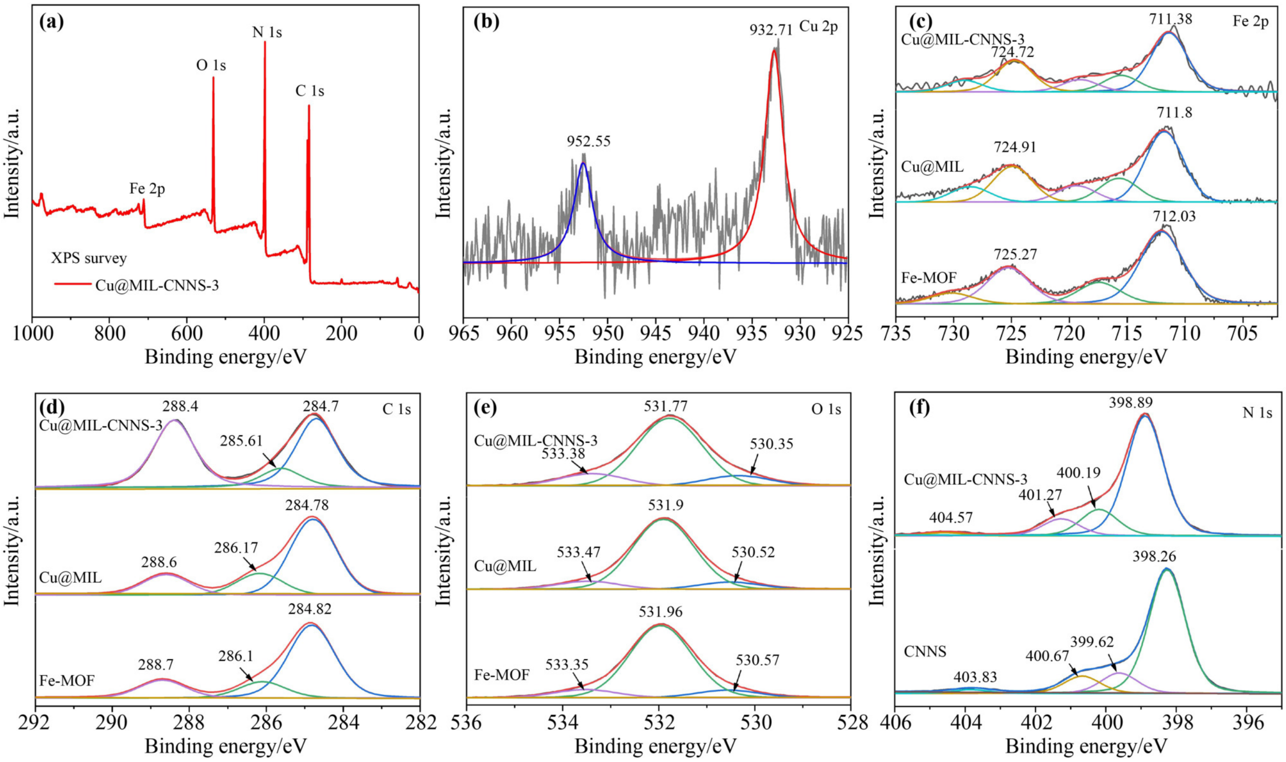

Fig. 3 (**a**) XPS survey spectrum and (**b**) Cu 2p XPS spectrum of Cu@MIL-CNNS-3. (**c**) Fe 2p, (**d**) C 1s, and (**e**) O 1s XPS spectra of three samples including Fe-MOF, Cu@MIL, and Cu@MIL-CNNS-3. (**f**) N 1s XPS spectra of two samples including Cu@MIL-CNNS-3 and CNNSs.

Cu@MIL and further to copper sites. Through the electron transfer, a close contact interface is formed between Cu@MIL and CNNSs in Cu@MIL-CNNS, which follows the charge transfer route of conventional Type II heterojunction.

Ultraviolet–visible diffuse reflectance spectroscopy (UV–Vis DRS) determines the absorption edges of various materials, which can be used to acquire bandgap (E_g) values. Figure 4(a) shows that the absorption edge of CNNSs is located in the wavelength range of 400–500 nm. For the Fe-MOF sample, two distinct visible absorption edges can be observed. It is noteworthy that the absorption fringes of Cu@MIL are red-shifted compared to Fe-MOF, indicating its improved ability to absorb visible light. After forming a composite with CNNSs, the visible absorption ability of the Cu@MIL-CNNS heterostructure is significantly enhanced. Particularly, Cu@MIL-CNNS-3 shows the most significant redshift, which effectively extends the visible light spectrum, thus contributing to the improvement of the photocatalytic activity. The E_g value of a sample can be calculated based on the Tauc plot, and the related equation is as follows:

$$\alpha h\nu = A\left(h\nu - E_g\right)^{n/2} \tag{1}$$

where α, $h\nu$, and A are the absorption coefficient, photon energy, and constant, respectively [51].

Both CNNSs and Fe-MOF are direct-transition semiconductors, so the value of n is 4. From E_g plots of the samples (Fig. 4(b)), it is seen that E_g values of CNNSs and Fe-MOF are 2.89 and 2.52 eV, respectively, and the bandgap was further narrowed to 2.40 eV after the introduction of copper ions. The energy band structure of Cu@MIL-NCN-3 was determined via X-ray photoelectron valence band spectroscopy (VB-XPS). The VB-XPS test results in Fig. 4(c) show that the valence band (VB) positions of CNNSs, Fe-MOF, and Cu@MIL are 1.72, 2.28, and 2.18 eV, respectively, relative to the normal hydrogen electrode. According to the VB values of the catalyst and equation [52]:

$$E_{\mathrm{CBM}} = E_{\mathrm{VBM}} - E_g \tag{2}$$

where E_{CBM} and E_{VBM} represent the CB potential and the VB potential, respectively.

The conduction band (CB) values of CNNSs, Fe-MOF, and Cu@MIL stand at −1.18, −0.24, and −0.22 eV,

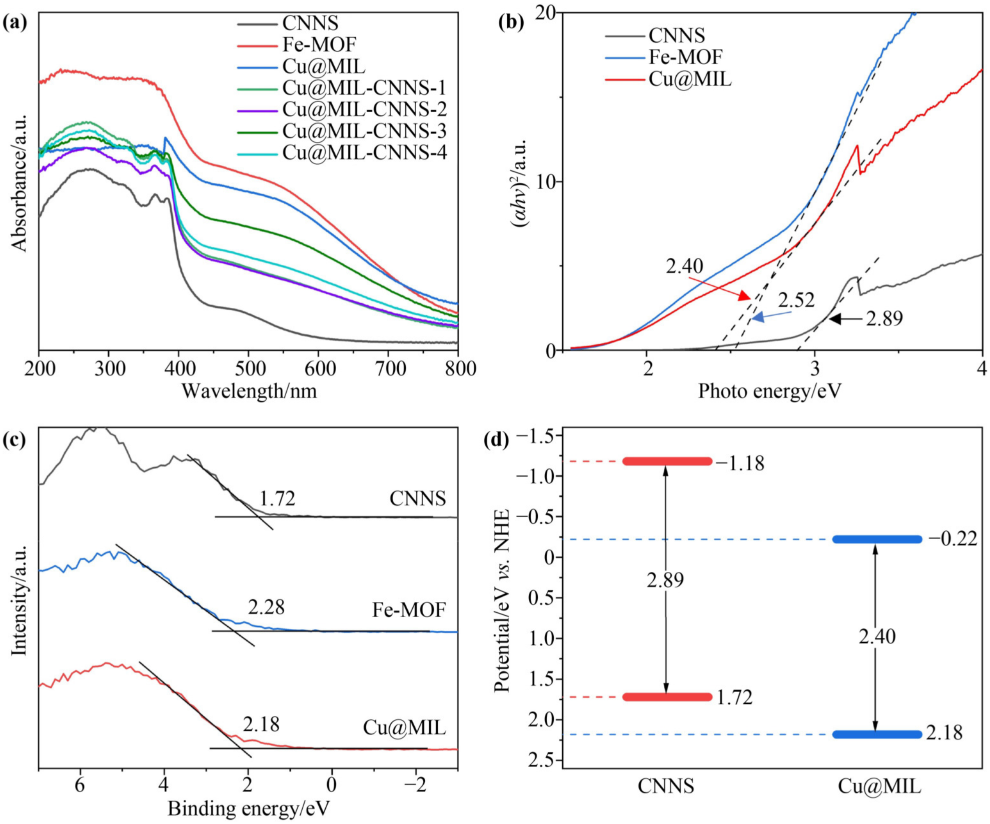

Fig. 4 (**a**) UV–Vis DRS curves of CNNSs, Fe-MOF, Cu@MIL, Cu@MIL-CNNS-1, Cu@MIL-CNNS-2, Cu@MIL-CNNS-3, and Cu@MIL-CNNS-4. (**b**) Different extrapolations to obtain bandgaps of CNNSs, Fe-MOF, and Cu@MIL from corresponding Tauc plots. (**c**) VB positions of CNNSs, Fe-MOF, and Cu@MIL. (**d**) Band structures of CNNSs and Cu@MIL.

respectively. Therefore, the schematic band structure evolution diagrams of CNNSs and Cu@MIL can be obtained, as shown in Fig. 4(d). The energy band arrangement of both satisfies the Type II heterojunction.

Photoelectrochemical (PEC) experiments show that compared to a single semiconductor, the photocurrent density of Cu@MIL-CNNS-3 is significantly higher due to the doping of copper ions and the presence of heterojunctions (Fig. 5(a)). In other words, there is enhanced photogenerated charge separation (CS) and higher transfer efficiency in the composite. More photogenerated electrons and holes are involved in the reaction, which is beneficial to the improvement in efficiency of photocatalytic nitrogen fixation. Figure 5(b) shows electrochemical impedance spectroscopy (EIS) Nyquist plots of tested samples, from which it is seen that Cu@MIL-CNNS has the lowest impedance, implying a low carrier migration resistance of the composite, which is favorable for CS. In this study, steady-state photoluminescence (PL) spectroscopy was performed to investigate various materials. Figure 5(c) shows that the PL spectrum of Fe-MOF has the most intense peak, which implies the highest rate of electron–hole recombination during the photocatalytic process. For Cu@MIL, the presence of copper is directly responsible for the significantly lowered PL intensity compared to that of Fe-MOF. The diminished luminescence intensity observed in Cu@MIL-CNNS implies that the heterojunction effectively inhibits the radiative relaxation process within the complex. This observation suggests a higher efficiency in separating electron–hole pairs, which aligns with its superior photocatalytic performance. Additionally, SSA values of photocatalysts were examined via the N_2 adsorption–desorption experiments. N_2 adsorption–desorption isotherms in Fig. 5(d) exhibit a consistent pattern, characterized by a Type IV isotherm curve with a H3-type hysteresis loop. This pattern indicates the presence of a typical mesoporous capillary cohesive structure featuring nanometer-scale spacing. The SSA values of CNNSs, Fe-MOF, and Cu@MIL-CNNS-3 heterostructures were measured to be 74.7, 58.1, and 95.6 $m^2 \cdot g^{-1}$, respectively. The greatly enhanced SSA of Cu@MIL-CNNS-3 effectively promotes the mass transfer between materials and improves the adsorption of N_2.

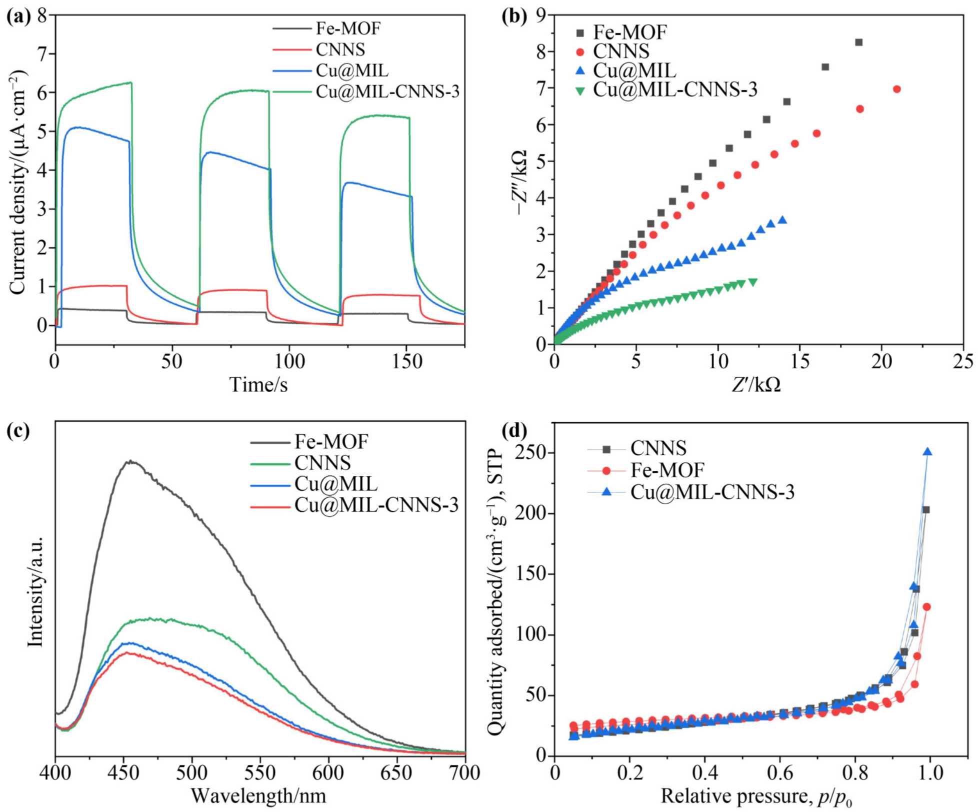

Fig. 5 (**a**) Transient photocurrent responses, (**b**) EIS Nyquist plots, and (**c**) room-temperature steady-state PL spectra of CNNSs, Fe-MOF, Cu@MIL, and Cu@MIL-CNNS-3. (**d**) N_2 adsorption–desorption isotherms of CNNSs, Fe-MOF, and Cu@MIL-CNNS-3.

3.2 Photocatalytic nitrogen fixation performance

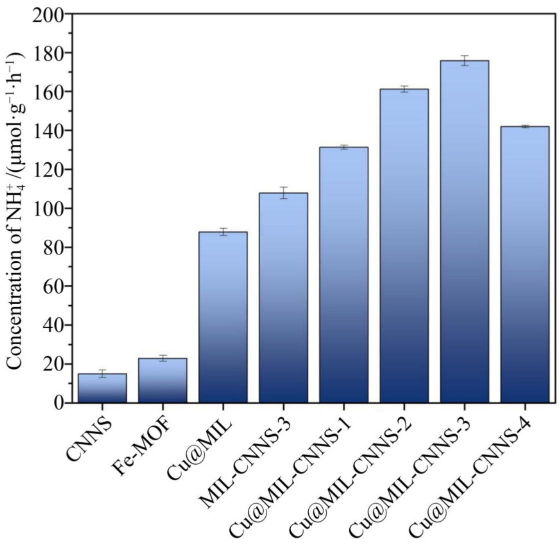

Fig. 6 Histogram of NH_4^+ production concentrations.

To elucidate the synergistic effect of single-atom copper loading and heterostructure construction on the ammonia synthesis, nitrogen fixation experiments were carried out under a simulated solar light source without the addition of any sacrificial agent and co-catalyst, and the NH_4^+ production rate was evaluated with a nitrogen aeration rate of 100 mL·min^{-1}. After purging with nitrogen for 30 min, the nitrogen reduction experiments were carried out under ambient conditions for 2 h. As depicted in Fig. 6, the original photocatalyst Fe-MOF presented a low nitrogen fixation efficiency (22.87 μmol·g^{-1}·h^{-1}), whereas the addition of copper ions resulted in an enhanced average nitrogen fixation efficiency (87.86 μmol·g^{-1}·h^{-1}) for Cu@MIL, nearly four times that for Fe-MOF, indicating the enhanced effect of photocatalytic nitrogen fixation. It is noteworthy that all prepared Cu@MIL-CNNS photocatalysts demonstrated significantly improved nitrogen fixation properties, in which Cu@MIL-CNNS-3 exhibited the highest nitrogen fixation efficiency of 175.83 μmol·g^{-1}·h^{-1}, approximately 8 and 12 times those of Fe-MOF and CNNSs, respectively, demonstrating superior performances of Cu@MIL-CNNS photocatalysts to those of single-component photocatalysts in terms of the nitrogen fixation efficiency. Furthermore, the nitrogen fixation efficiency of Cu@MIL-CNNS-3 was 1.6 times that of MIL-CNNS-3 without copper ions and 2 times that of Cu@MIL, indicating that the synergistic effect of copper single atoms and heterojunctions is crucial for superior photocatalytic nitrogen fixation. These results clearly demonstrate the significant contribution of the copper single-atom loading and heterostructure construction to the photocatalytic nitrogen fixation activity of Cu@MIL-CNNS photocatalysts.

The enhanced photocatalytic performances of Cu@MIL-CNNS composites can be attributed to the synergistic effect within the materials. First, the well-connected and tightly bonded heterojunction formed between Cu@MIL and CNNSs can effectively absorb light and promote the conversion of absorbed light into photogenerated charge carriers. Secondly, the presence of single-atom copper sites can act as active centers to enhance the capturing of photogenerated electrons and promote the nitrogen fixation reaction during photocatalysis. PEC results depicted in Figs. 5(a)–5(c) corroborate aforementioned propositions, with Cu@MIL-CNNS-3 showing the highest EIS value, the most sensitive photocurrent response, and the lowest recombination degree of photogenerated carriers. These findings reveal that Cu@MIL-CNNS-3 has good PEC properties, which are essential for the improvement of photocatalytic performance.

Meanwhile, the photocatalytic stability of the Cu@MIL-CNNS-3 composite was verified through a five-consecutive-cycle experiment. As shown in Fig. S4 (included by ESM of Appendix), the amount of fixed nitrogen remained fairly consistent over five cycles, implying that the Cu@MIL-CNNS-3 composite is stable and durable during the photocatalytic nitrogen fixation reaction. Characterization measurements of recovered samples reveal the same microstructures before and after the cycling tests, further indicating the high stability of Cu@MIL-CNNS during the nitrogen fixation. In addition, the effectiveness of the photocatalytic activity was verified via a comparative analysis. Notably, no ammonia gas was detected either in the absence of photocatalyst and incident light or in the presence of argon atmosphere, as shown in Fig. S6 (included by ESM of Appendix), indicating that nitrogen is an indispensable factor for photoreduction, because the ammonia gas derived during the photocatalytic nitrogen fixation is from the nitrogen gas. The nitrogen fixation rate of Cu@MIL-CNNS-3 was also compared with those of some recently reported MOF heterojunction photocatalysts as well as metal-doped materials, and the results are summarized in Table S1 (included by ESM of Appendix), in which Cu@MIL-CNNS-3 was found to have the highest nitrogen fixation capacity among all listed samples.

3.3 Possible photocatalytic mechanism

Based on above experiments and analyses, possible reactions transpiring amidst the photocatalytic nitrogen fixation are delineated according to Eqs. (3)–(7) as follows:

$$\text{Cu@MIL-CNNS} + h\nu \rightarrow \text{h}^+(\text{VB}, \text{CNNS}) + \text{e}^-(\text{CB}, \text{Cu@MIL}) \tag{3}$$

$$\text{Cu@MIL(e)}^- + \text{Cu} \rightarrow \text{Cu(e)}^- + \text{Cu@MIL} \tag{4}$$

$$2\text{H}_2\text{O} + 4\text{h}^+ \rightarrow 4\text{H}^+ + \text{O}_2 \tag{5}$$

$$\text{N}_2 + 6\text{e}^- + 6\text{H}^+ \rightarrow 2\text{NH}_3 \tag{6}$$

$$\text{NH}_3 + \text{H}_2\text{O} \rightarrow \text{NH}_4^+ + \text{OH}^- \tag{7}$$

Also, the mechanism of the photocatalytic nitrogen fixation in Cu@MIL-CNNS composites can be explained, as shown in Fig. 7. The Type-II heterostructure formed by Cu@MIL-CNNS can effectively separate the electron–hole pairs, while electrons with high reduction potential can effectively promote the nitrogen fixation reaction. As both CNNSs and iron-based MOFs prepared are nanomaterials, their unique nanostructures have size-constraining effect on active substances involved in the reaction, leading to their size in a specific nanometer range. Meanwhile, the transport distance of carriers is shortened, thus effectively inhibiting the recombination of electrons and holes during the reaction [53]. Under the irradiation of visible light, electrons in VB are excited followed by the leap to CB, leaving holes in VB. According to the band structure shown in Fig. 7, the VB value of CNNSs is −1.18 eV, more negative than that of Cu@MIL (−0.22 eV). Therefore, when CNNSs and Cu@MIL are in close contact, photogenerated electrons can be transferred from the CB of CNNSs to the CB of Cu@MIL through the heterojunction structure, consistent with the results from XPS. Subsequently, holes are also transferred from the VB of Cu@MIL to the VB of

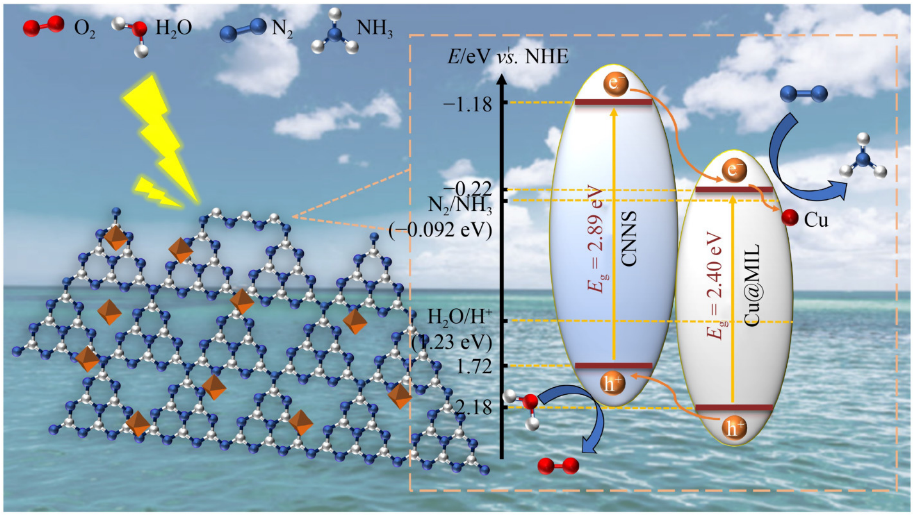

Fig. 7 Possible route for charge transfer and reaction mechanism of nitrogen photofixation.

CNNSs. Photogenerated electrons on the CB of Cu@MIL and photogenerated holes on the VB of CNNSs are involved in the reduction process of nitrogen (Eq. (6)) and the oxidation process of water (Eq. (5)), respectively. This greatly promotes the separation efficiency of electron–hole pairs, improving the performance of the photocatalytic nitrogen fixation.

Building upon the foregoing analytical endeavors, we postulate a fitting mechanistic framework for the Cu@MIL-CNNS photocatalyst, categorized under the rubric of a Type-II heterojunction. The CB potential of Cu@MIL surpasses the reduction potential of N_2/NH_3 (−0.092 eV), while the VB potential of CNNSs is lower than the oxidation potential of H_2O/H^+ (1.23 eV). This arrangement ensures that the heterojunction possesses ample energy to facilitate the reduction from N_2 to NH_3, generating electrons and protons. In addition, copper atoms in Cu@MIL-CNNS can mobilize the electronic band structure and narrow the bandgap of iron-based MOF, retaining high energy-photoexcited electrons on the CB for the reduction of nitrogen, while copper ions themselves provide a great number of active sites for the adsorption and activation of nitrogen. Electrons in the CB of Cu@MIL, as the main active species, can be rapidly involved in the nitrogen reduction reaction (NRR).

4 Conclusions

In summary, a novel Cu@MIL-CNNS composite catalyst was successfully designed and synthesized in this study via a facile hydrothermal and calcination method to realize an efficient visible-light-driven nitrogen fixation reaction. Notably, Cu@MIL-CNNS, which was modulated with energy band structure and formed a heterogeneous structure, possessed excellent photocatalytic activity, and its nitrogen fixation efficiency was 12 and 8 times those of CNNSs alone and Fe-MOF alone, respectively. The single-atom copper provides active sites and modulation of the MOF bandgap, and the formation of heterostructures accelerates charge separation and transfer. This synergistic effect gives this composite a remarkable redox capacity that promotes the adsorption and activation of nitrogen. These findings not only demonstrate the potential of constructing photocatalysts composed of monolithic atoms and heterostructures, but also provide valuable insights into the design of efficient photocatalytic nitrogen fixation systems.

Authors' contributions Xinshan Rong: conceptualization, supervision, and writing — review & editing; Yuqing He: data curation and original draft writing; Ping Gao: methodology and visualization; Ting Sun: data curation and visualization; Xiangtong Zhou: methodology; Zhiren Wu: methodology and visualization.

Declaration of competing interests The authors declare that they have no known competing financial interests or personal relationships that could have appeared to influence the work reported in this paper.

Acknowledgements This work was financially supported by the National Natural Science Foundation of China (Grant No. 22005125) and the Jiangsu Collaborative Innovation Center of Technology and Material of Water Treatment.

Data availability statement The authors confirm that the data supporting the findings of this study are available within the article.

Online appendix Electronic supplementary material (ESM) can be found in the online version at https://doi.org/10.1007/s11706-024-0702-z and https://journal.hep.com.cn/foms/EN/10.1007/s11706-024-0702-z that includes Table S1 and Figs. S1–S6.

References

[1] Zhang D, He W, Ye J, et al. Polymeric carbon nitride-derived photocatalysts for water splitting and nitrogen fixation. Small, 2021, 17(13): 2005149

[2] Rong X, Chen H, Rong J, et al. An all-solid-state Z-scheme $TiO_2/ZnFe_2O_4$ photocatalytic system for the N_2 photofixation enhancement. Chemical Engineering Journal, 2019, 371: 286−293

[3] Prabagar J S, Sneha Y, Tenzin T, et al. Photocatalytic transfer of aqueous nitrogen into ammonia using nickel–titanium-layered double hydroxide. Environmental Science and Pollution Research, 2023, 30(39): 90341−90351

[4] Ding Z, Sun M, Liu W, et al. Ultrasonically synthesized N-TiO_2/Ti_3C_2 composites: enhancing sonophotocatalytic activity for pollutant degradation and nitrogen fixation. Separation and Purification Technology, 2021, 276: 119287

[5] Hui X C, Li L F, Xia Q N, et al. Interface engineered $Sb_2O_3/W_{18}O_{49}$ heterostructure for enhanced visible-light-driven photocatalytic N_2 reduction. Chemical Engineering Journal, 2022, 438: 135485

[6] Chang M J, Zhang C M, Li W J, et al. Significantly enhanced the light absorption and charge separation of $Bi_{0.5}Na_{0.5}TiO_3$ by coupling with CdS for high-performance piezo-photocatalysis. Environmental Science and Pollution Research International, 2023, 30(50): 109410−109422

[7] Zhang C, Chen G, Lv C, et al. Enabling nitrogen fixation on Bi_2WO_6 photocatalyst by c-PAN surface decoration. ACS Sustainable Chemistry & Engineering, 2018, 6(9): 11190−11195

[8] Liu J, Li F, Lu J, et al. Atomically dispersed palladium–ethylene glycol–bismuth oxybromide for photocatalytic nitrogen fixation: insight of molecular bridge mechanism. Journal of Colloid and Interface Science, 2021, 603: 17−24

[9] Zhang C J, Liang Q, Wang Y A, et al. Construction of Z-scheme heterojunction CoS/CdS@g-C_3N_4 hollow sphere with spatical charge separation for enhanced photocatalytic hydrogen production. Applied Surface Science, 2023, 626: 157214

[10] Zhou X, Hwang I, Tomanec O, et al. Advanced photocatalysts: pinning single atom Co-catalysts on titania nanotubes. Advanced Functional Materials, 2021, 31(30): 2102843

[11] Zhang C X, Xie C F, Gao Y Y, et al. Charge separation by creating band bending in metal–organic frameworks for improved photocatalytic hydrogen evolution. Angewandte Chemie International Edition, 2022, 61(28): e202204108

[12] Zhang Y, Xu J, Zhou J, et al. Metal–organic framework-derived multifunctional photocatalysts. Chinese Journal of Catalysis, 2022, 43(4): 971−1000

[13] Qian Y, Zhang F, Pang H. A review of MOFs and their composites-based photocatalysts: synthesis and applications. Advanced Functional Materials, 2021, 31(37): 2104231

[14] Hu J, Ji Y, Mo Z, et al. Engineering black phosphorus to porous g-C_3N_4–metal–organic framework membrane: a platform for highly boosting photocatalytic performance. Journal of Materials Chemistry A: Materials for Energy and Sustainability, 2019, 7(9): 4408−4414

[15] Jin J, Wan S, Lee S, et al. Tailoring the nanoporosity and photoactivity of metal–organic frameworks with rigid dye modulators for toluene purification. Small, 2023, 19(39): 2302776

[16] Wang C H, Wan Y Y, Yang S K, et al. Revealing the untapped potential of photocatalytic overall water splitting in metal organic frameworks. Advanced Functional Materials, 2024, 34(13): 2313596

[17] Liu Z, Chen Z, Li M, et al. Construction of single Ni atom-immobilized ZIF-8 with ordered hierarchical pore structures for selective CO_2 photoreduction. ACS Catalysis, 2023, 13(10): 6630−6640

[18] Wang S, Zhang J J, Zong M Y, et al. Energy level engineering: Ru single atom anchored on Mo-MOF with a $[Mo_8O_{26}(im)_2]^{4-}$ structure acts as a biomimetic photocatalyst. ACS Catalysis, 2022, 12(13): 7960−7974

[19] Johnson E M, Boyanich M C, Gibbons B, et al. Aqueous-phase destruction of nerve-agent simulants at copper single atoms in UiO-66. Inorganic Chemistry, 2022, 61(22): 8585−8591

[20] Chen S, Zhou Y, Li J, et al. Single-atom Ru-implanted metal–organic framework/MnO_2 for the highly selective oxidation of NO_x by plasma activation. ACS Catalysis, 2020, 10(17): 10185−10196

[21] Haider S N U Z, Qureshi W A, Ali R N, et al. Contemporary advances in photocatalytic CO_2 reduction using single-atom catalysts supported on carbon-based materials. Advances in Colloid and Interface Science, 2024, 323: 103068

[22] Ma S, Han W, Han W, et al. Recent advances and future perspectives in MOF-derived single-atom catalysts and their application: a review. Journal of Materials Chemistry A: Materials for Energy and Sustainability, 2023, 11(7): 3315−3363

[23] Qu W, Chen C, Tang Z Y, et al. Progress in metal–organic-framework-based single-atom catalysts for environmental remediation. Coordination Chemistry Reviews, 2023, 474:

214855

[24] Chen D M, Sun C X, Liu C S, et al. Stable layered semiconductive Cu(I)–organic framework for efficient visible-light-driven Cr(VI) reduction and H_2 evolution. Inorganic Chemistry, 2018, 57(13): 7975−7981

[25] Chimupala Y, Kaeosamut N, Yimklan S. Octahedral to tetrahedral conversion upon a ligand-substitution-induced single-crystal to single-crystal transformation in a rectangular Zn(II) metal–organic framework and its photocatalysis. Crystal Growth & Design, 2021, 21(9): 5373−5382

[26] Qin Y, Hao M, Wang J, et al. Rational design of a core–shell structured plasmonic Au@MIL-100(Fe) nanocomposite for efficient photocatalysis. ACS Applied Materials & Interfaces, 2022, 14(51): 56930−56937

[27] Melillo A, García-Aboal R, Navalón S, et al. Photoactive Zr and Ti metal–organic-frameworks for solid-state solar cells. ChemPhysChem, 2021, 22(9): 842−848

[28] Yi X H, Ma S Q, Du X D, et al. The facile fabrication of 2D/3D Z-scheme g-C_3N_4/UiO-66 heterojunction with enhanced photocatalytic Cr(VI) reduction performance under white light. Chemical Engineering Journal, 2019, 375: 121944

[29] Tang C, Ma S Q, Yi X H, et al. MIL-88A(Fe)/TCNQ composites for boosted photo-Fenton sulfamethoxazole degradation under LED visible light. Materials Research Bulletin, 2023, 160: 112138

[30] Chen X, Pan W G, Guo R T, et al. Recent progress on van der Waals heterojunctions applied in photocatalysis. Journal of Materials Chemistry A: Materials for Energy and Sustainability, 2022, 10(14): 7604−7625

[31] Zhang Q, Sun Y, Deng J, et al. Defect-rich selenium doped graphitic carbon nitride for high-efficiency hydrogen evolution photocatalysis. International Journal of Hydrogen Energy, 2023, 48(81): 31590−31598

[32] Ma A S, Qian H L, Liu H X, et al. Degradation of malachite green by g-C_3N_4-modified magnetic attapulgite composites under visible-light conditions. Environmental Science and Pollution Research, 2023, 30(42): 96360−96375

[33] Purohit S, Singh S, Yadav K L, et al. Enhanced CO_2 reduction with $Cs_2AgBiBr_6$–gC_3N_4 heterojunction photocatalysts prepared by green synthesis. ACS Applied Energy Materials, 2023, 6(10): 5580−5587

[34] Yi X H, Wang F X, Du X D, et al. Facile fabrication of BUC-21/g-C_3N_4 composites and their enhanced photocatalytic Cr(VI) reduction performances under simulated sunlight. Applied Organometallic Chemistry, 2019, 33(1): e4621

[35] Cheng C, Chen D, Li N, et al. NH_2-MIL-125(Ti) modified graphitic carbon nitride with carbon vacancy for efficient photocatalytic NO removal. Chemosphere, 2022, 307: 135660

[36] Lei Z D, Xue Y C, Chen W Q, et al. The influence of carbon nitride nanosheets doping on the crystalline formation of MIL-88B(Fe) and the photocatalytic activities. Small, 2018, 14(35): 1802045

[37] Wang X W, Zhu L F, Lv Z W, et al. Coupled visible-light driven photocatalytic reactions over porphyrin-based MOF materials. Chemical Engineering Journal, 2022, 442: 136186

[38] Luo T, Gilmanova L, Kaskel S. Advances of MOFs and COFs for photocatalytic CO_2 reduction, H_2 evolution and organic redox transformations. Coordination Chemistry Reviews, 2023, 490: 215210

[39] Ma Y, Lu Y, Hai G, et al. Bidentate carboxylate linked TiO_2 with NH_2-MIL-101(Fe) photocatalyst: a conjugation effect platform for high photocatalytic activity under visible light irradiation. Science Bulletin, 2020, 65(8): 658−669

[40] An S, Guo Y, He X, et al. Intermediate-induced repolymerization for constructing self-assembly architecture: red crystalline carbon nitride nanosheets for notable hydrogen evolution. Applied Catalysis B: Environmental, 2022, 310: 121323

[41] Sun T, Gao P, Zhang S, et al. 3D porous carbon nitride composited oxygen vacancy-induced indium oxide for high photocatalytic nitrogen fixation on the interfacial surface. Applied Organometallic Chemistry, 2023, 37(7): e7117

[42] Xu J, Qi Y, Wang C, et al. NH_2-MIL-101(Fe)/Ni$(OH)_2$-derived C,N-codoped Fe_2P/Ni_2P cocatalyst modified g-C_3N_4 for enhanced photocatalytic hydrogen evolution from water splitting. Applied Catalysis B: Environmental, 2019, 241: 178−186

[43] Sun D R, Liu W J, Qiu M, et al. Introduction of a mediator for enhancing photocatalytic performance via post-synthetic metal exchange in metal–organic frameworks (MOFs). Chemical Communications, 2015, 51(11): 2056−2059

[44] Song Y P, He L N, Zhang S, et al. Novel impedimetric sensing strategy for detecting ochratoxin A based on NH_2-MIL-101(Fe) metal–organic framework doped with cobalt phthalocyanine nanoparticles. Food Chemistry, 2021, 351: 129248

[45] Ma Y, Zhang Y, Ma Y, et al. *In situ* Cu single atoms anchoring on MOF-derived porous TiO_2 for the efficient separation of photon-generated carriers and photocatalytic H_2 evolution. Nanoscale, 2022, 14(42): 15889−15896

[46] Büker J, Huang X, Bitzer J, et al. Synthesis of Cu single atoms supported on mesoporous graphitic carbon nitride and their application in liquid-phase aerobic oxidation of cyclohexene. ACS Catalysis, 2021, 11(13): 7863−7875

[47] Xu Q, Sun Y, Lv T, et al. Selective CO_2 photoreduction into CO

over Ti_3C_2 quantum dots decorated NH_2-MIL-101(Fe) heterostructures. Journal of Alloys and Compounds, 2023, 954: 170088

[48] Wang H, Tu H, Chen F, et al. Construction of highly dispersed NH_2-MIL-101(Fe)/g-C_3N_4 heterostructure with excellent photocatalytic redox capability. Journal of Environmental Chemical Engineering, 2023, 11(3): 109663

[49] Dao X Y, Xie X F, Guo J H, et al. Boosting photocatalytic CO_2 reduction efficiency by heterostructures of NH_2-MIL-101(Fe)/g-C_3N_4. ACS Applied Energy Materials, 2020, 3(4): 3946−3954

[50] An S F, Zhang G H, Li K Y, et al. Self-supporting 3D carbon nitride with tunable $n \rightarrow \pi^*$ electronic transition for enhanced solar hydrogen production. Advanced Materials, 2021, 33(49): 2104361

[51] Bi X Y, Li L B, Luo L J, et al. A ratiometric fluorescence aptasensor based on photoinduced electron transfer from CdTe QDs to WS_2 NTs for the sensitive detection of zearalenone in cereal crops. Food Chemistry, 2022, 385: 132657

[52] Xu Y H, Wen Z R, Wang T S, et al. Ternary Z-scheme heterojunction of Bi SPR-promoted $BiVO_4$/g-C_3N_4 with effectively boosted photoelectrochemical activity for constructing oxytetracycline aptasensor. Biosensors & Bioelectronics, 2020, 166: 112453

[53] Zhou H X, Hu Y B, Zhang Y, et al. Rational design of materials for CO_2 photoreduction to yield C_{2+} products. Separation and Purification Technology, 2025, 359: 130549